

This is a postprint version of the following published document:

Del Campo, R., Savoini, B., Muñoz, A., Monge, M. A., & Pareja, R. (2017). Processing and mechanical characteristics of magnesium-hydroxyapatite metal matrix biocomposites. *Journal of the Mechanical Behavior of Biomedical Materials*, 69, 135-143

DOI: <https://doi.org/10.1016/j.jmbbm.2016.12.023>

© Elsevier, 2017



This work is licensed under a [Creative Commons Attribution-NonCommercial-NoDerivatives 4.0 International License](https://creativecommons.org/licenses/by-nc-nd/4.0/).

PROCESSING AND MECHANICAL CHARACTERISTICS OF MAGNESIUM-HYDROXYAPATITE METAL MATRIX BIOCOMPOSITES

R. del Campo^a, B. Savoini^{a,b}, A. Muñoz^{a,b}, M. A. Monge^{a,b}, R. Pareja^{a,b}

¹Universidad Carlos III de Madrid, Departamento de Física, Avda. de la Universidad 30, 28911, Leganés, Spain.

²Instituto Tecnológico de Química y Materiales Alvaro Alonso Barba (IAAB), Avda. Universidad 30, 28911, Leganés, Spain.

Abstract

Magnesium/hydroxyapatite composites were produced by conventional extrusion and their mechanical behavior studied under uniaxial compression at room temperature. The results evidence the capability of the HA for strengthening the Mg material, lowering its microstructural anisotropy and inhibiting deformation twinning. They also reveal that the ECAP processing is effective for improving the grain structure and reducing the crystallographic texture of these composites, giving rise to a significant enhancement of their yield strength and microhardness although the ultimate compressive stress worsens. The analysis of the strain hardening rate of the flow curves demonstrates that the HA addition and the ECAP processing are also effective in inhibiting non-basal dislocation slip.

Keywords: biocomposite; magnesium; hydroxyapatite; strain hardening; texture hardening

1. Introduction

Magnesium is a biocompatible, osteoconductive, osseointegrable and lightweight material with mechanical properties quite similar to bone tissue that can be used for load-bearing degradable implants replacing advantageously other metallic biomaterials. Magnesium, as an essential cofactor of the alkaline phosphatase isozymes, may effectively contribute to the healing or remodeling of bone tissue. Moreover, it has

superior fracture toughness and a Young modulus closer to the one of nature bone than synthetic hydroxyapatite (HAP), $\text{Ca}_{10}(\text{PO}_4)_6(\text{OH})_2$, or other bioceramics. The behavior of diverse magnesium-based materials as biomaterial has been reported and some of their restrictive issues identified (Atrens et al., 2011; Staiger et al., 2006; Witte, 2010). Magnesium is very susceptible to corrosion and decomposes very fast under *in vivo* conditions causing intrusive gas release and failure of the implants before achieving the envisaged effect in the receptor (Staiger et al., 2006; Virtanen, 2011; Witte et al., 2005; Witte et al., 2008). Then, load-bearing degradable implants require magnesium based materials with reduced corrosion rates that preserve their mechanical reliability during the period of bone fixation until the complete resorption. HA reinforced magnesium matrix composites appear to be ideal materials for designing such implants with adjustable corrosion resistance and mechanical properties. This reinforcement phase besides reducing the corrosion rate is highly insoluble in the physiological environment of bone tissue and may enhance the mechanical resistance (del Campo et al., 2014; Gu et al., 2010; Mensah-Darkwa et al., 2013; Witte et al., 2007). Furthermore, non-toxic elements would release in the case of a pure magnesium matrix. The current commercial magnesium alloys, which were not developed for medical applications, contain alloying impurities such as Al, Zn, Zr, Ca, Li, Y and RE to enhance the mechanical properties and corrosion resistance in an environment quite different to the corresponding to a living organism (Li et al., 2008; Neubert et al., 2007; Song, 2007; Sun et al., 2009). The corrosion reaction of these alloys in the physiological environment can release the alloying impurities resulting in a detrimental effect on their cytocompatibility and mechanical properties. In order to progress in knowledge of the biodegradable magnesium materials and contribute to the development of pure magnesium matrix-HAP composites, the effect of their processing route on the mechanical properties, corrosion resistance and cytocompatibility deserves to be investigated.

The present paper reports the microstructural and mechanical characteristics of pure magnesium-HAP composites produced by conventional extrusion, and subsequent equal channel angular pressing (ECAP) to modify its microstructure and improve the mechanical properties. The *in vitro* studies of corrosion and cytocompatibility for these materials will be reported elsewhere.

2. Experimental

2.1. Processing of the magnesium-HA composites

Magnesium- x HA composites with $x=5, 10$ and 15 wt % (2.9, 5.9 and 9.0 vol %) were fabricated following different powder metallurgy routes. The starting powders were 99.8% pure magnesium with average particle size of $38\ \mu\text{m}$ supplied by Alfa Aesar, and high purity synthetic HA powder supplied either by Berkeley Advanced Biomaterials (BABI-HAP-P mesh -100) with an average particle size of $25\ \mu\text{m}$ and Ca/P ratio of 1.64, or Plasma Biotal Ltd. (Captal 'S' HA) with a Ca/P ratio of 1.67 and average size of $6\ \mu\text{m}$. Powders with the target compositions were blended for 6 h in a Turbula Wab mixer and compacted in silicone moulds by cold isostatic pressing at 250 MPa pressure for 5 min. The compacts were consolidated by conventional extrusion at $400\ ^\circ\text{C}$ with a extrusion ratio $R=11$ and a final diameter of 10 mm. The extrusion rates were 120 mm/min for the composites with Berkeley HA (labeled as L-xHAP) and 30 mm/min for the composites with Plasma HA (labeled as S-xHAP). $\varnothing 8\ \text{mm} \times 120\ \text{mm}$ cylindrical rods, machined from the consolidates billets of the L-xHAP composites, were ECAP processed at $300\ ^\circ\text{C}$ and 30 mm/min through a die with an intersection angle of 105° for 4 passes following the so-called route B_C . Route B_C consists in rotating the billet $+90^\circ$ around its longitudinal axis in the same direction before inserting in the die for the subsequent pass. The materials processed by ECAP were labeled as LE-xHAP.

2.2. Microstructural and mechanical characterization

The consolidation grade of the composites was quantified by the ratio between the density measured in a He ultracycrometer and the theoretical density calculated applying the mixture rule. The microstructure of the composites was examined by optical and scanning electron microscopy (SEM) and energy dispersive spectroscopy (EDS). Moreover, crystallography texture measurements were carried out applying the Schulz reflection method in a Siemens TM Kristalloflex D5000 diffractometer equipped with a eulerian cradle. The reference system for the samples maintained the Z-axis along the extrusion direction, is shown in Figure 1. The orientation distribution functions (ODFs) were obtained from the measurements of the (0002) , $(10\bar{1}0)$, $(10\bar{1}2)$ and $(11\bar{2}0)$ pole figures taken at X - Y sections. In order to characterize the

sharpness of the texture by a single parameter, the texture index J was determined for each sample. It is calculated by the integral of the square of the texture function and it varies between 1 for a completely random orientation and ∞ for an ideal single crystal (Bunge, 2015).

Vickers microhardness measurements were performed on the parallel (X - Z planes) and normal (X - Y planes) sections to the extrusion axis of the samples applying a load of 9.81 N for 20 s. At least 10 indentations were made to obtain the microhardness mean value. Room temperature uniaxial compression tests at a constant strain rate of 10^{-4} s^{-1} were performed on $\varnothing 6 \text{ mm} \times 10.5 \text{ mm}$ cylindrical samples machined with their longitudinal axis along the extrusion direction. Barrelling of the samples during the compression tests was effectively inhibited applying hexagonal BN powder as lubricant between the compression platens and the ends of the samples.

For the microstructure and compositional analyses, as well for the mechanical characterization, the samples were abraded using SiC papers and carefully polished with α -alumina slurry ($0.3 \mu\text{m}$) and cloths. The optical and electron microscopy images were taken after etching the samples for 5 s in a solution of 1.5 g of picric acid, 25 ml of ethanol, 5 ml acetic acid and 10 ml of distilled water.

3. Results and discussion

3.1. Microstructure and crystallographic texture

Figures 2 and 3 show the microstructure of pure S-Mg and the S-xHAP composites in the as-extruded conditions. In the case of pure S-Mg, the consolidation extrusion under the present conditions caused a grain structure composed of grains elongated along the extrusion direction with typical lengths of 20 – 50 μm and widths of $\sim 3 \mu\text{m}$ giving rise to the expected $(10\bar{1}0)$ fiber texture, as the experimental pole figures in Figure 4 reveal. The calculated orientation distribution functions (ODFs) for S-Mg and S-15HAP represented in Figure 5 exemplify the texture changes induced by the HA addition. The HA addition increased meaningfully the grain width reducing the aspect ratio from 14 to a typical value of ~ 6 , and the texture index J from 5.55 to 2.20 (see Figure 4 and Table 1). The HA phase, which appears as dark inclusions in the optical images, or light grey in the SEM images, is found quite homogeneously distributed.

Their sizes range from less of 1 μm to $\sim 30 \mu\text{m}$. The smaller particles appear preferentially alongside the boundaries of the elongated grains besides inside the Mg grains, as it can be shown in Figure 3d). On the contrary, the larger particles partially tend to cluster together in groups, Figure 3c). In addition to HA particles, the EDS analyses revealed a small presence of MgO particles with typically submicron sizes.

The effect of the ECAP processing on the microstructure and texture of the Mg/HA composites are summarized in Table 1. Since the ECAP processed composites, i.e. the LE-xHAP samples, were prepared with HA powder from different supplier and rougher than the one used for the S-xHAP composites, the results for the counterpart non-ECAP processed composites (L-xHAP) reported in Ref. (del Campo et al., 2014) are also included for comparison in Table 1. Figures 6 and 7 show the grain structure and HA phase distribution in ECAP processed composites. As the starting HA powder used for these samples was rougher, the HA particles result to be less homogeneously distributed and their sizes up to $\sim 25 \mu\text{m}$ compared with S-xHAP composites. The reduction of the grain lengths by ECAP deformation without meaningful effect on the grain widths, resulting in a significant change in the aspect ratio of the grains, is clear as the images of Figures 6 and 7 and the data in Table 1 reveal. Moreover, the ECAP processing produced the effective destruction of the initial fiber texture of the Mg/HA composites. This is apparently assisted by the HA content as the pole figures in Figure 8 show. The calculated ODFs for LE-5HAP and LE-15HAP represented in Figure 9, in combination with the ODFs in Figures 5, show the texture changes induced by ECAP deformation.

3.2. Mechanical characterization

Figures 10 and 11 depict the stress-strain curves of the uniaxial compression tests for the S-xHAP composites and the ECAP deformed LE-xHAP composites, along with those for Mg pure samples extruded under the corresponding conditions to the composites. The results are summarized together with the microstructural characteristics in Table 1. All the flow stress curves exhibit the characteristic concave shape respect the upper compression stress (UCS) revealing the formation of $(10\bar{1}2)$ deformation twins (Barnet et al., 2004; Kelley and Hosford, 1968; Sarker et al., 2015). It is clear noticed from the stress-strain curves and the texture index given in Table 1 that the ECAP processing, besides destroying the original fiber texture, lowers the concave upwards shape of the flow curves. The Mg/HA composites in general exhibit better mechanical

properties that the extruded Mg samples. In the S-xHAP composites, increasing the HA fraction the UCS value and the yield strength apparently increase. On the contrary, in the ECAP deformed LE-xHAP composites the UCS drops while the yield strength rises, appreciably.

Furthermore, it is found that the microhardness values increase linearly with the HA fraction and the inverse of the texture index J as Figures 12 and 13 show. Figure 13 reveals anisotropy in the microhardness when the J value is above 2. It is also apparent that the ECAP deformation reduced the J values below 2. It is worth noticing that the microhardness increasing rate with J^{-1} is virtually independent of measurement plane as the plots in Figure 13 for the S-xHAP and L-xHAP composites in the as-extruded condition reveal. They result in increasing rates of 213 ± 19 and 235 ± 24 MPa for the S-xHAP samples in the transversal (X - Y) and longitudinal (X - Z) planes, respectively, and 223 ± 21 and 280 ± 60 MPa for the L-xHAP samples. Besides destroying the microhardness anisotropy, the ECAP processing rises the microhardness and its increasing rate with J^{-1} . These rates were respectively 1020 ± 120 and 830 ± 60 MPa in the transversal (X - Y) and longitudinal (X - Z) planes. An interpretation of microhardness dependence on J^{-1} will be given later on.

3.2. Discussion

Although the L-xHAP composites exhibit a quiet inhomogeneous distribution of the HA reinforcement and a microstructure worse than the one developed in the S-xHAP composites, the compressive properties and microhardness are unexpectedly better. This is attributed to a profuse presence of other secondary phase identified as MgO by EDS analyses in the L-xHAP samples (del Campo et al., 2014). The less controlled extrusion processing of the L-xHAP composites may be responsible for abundant formation of the MgO phase resulting in a higher fraction of reinforcement particles in the composites.

To get insight on the mechanical behavior of these Mg/HA composites the compression flow curves have been analyzed using the Kocks-Mecking approach (Kocks and Mecking, 2003) according to the terms applied for magnesium alloys in Refs. (Cáceres and Blake, 2007; Cáceres et al., 2008; Figueiredo et al., 2010). This has

been accomplished via the representation of the $(\sigma - \sigma_0) \frac{d\sigma}{d\varepsilon}$ versus $(\sigma - \sigma_0)$, where σ_0 is the yield strength value and $\frac{d\sigma}{d\varepsilon}$ the strain hardening rate derived from the polynomial fits of the flow curves in the strain range between the yield strength and the UCS for each material. The stress at the lower yield point of the corresponding flow curve was taken as the yield strength value of the material.

For polycrystalline materials $(\sigma - \sigma_0) \frac{d\sigma}{d\varepsilon}$ can be described expressed as (Cáceres and Blake, 2007; Cáceres et al., 2008)

$$(\sigma - \sigma_0) \frac{d\sigma}{d\varepsilon} = (\sigma - \sigma_0) [\Theta_h - \Theta_r(\sigma, \varepsilon, T)] \quad (1)$$

where Θ_h represents the athermal contribution of the dislocations to the strain hardening rate, and Θ_r the softening due to dynamic recovery. In absence of dynamic recovery, the $(\sigma - \sigma_0) \frac{d\sigma}{d\varepsilon}$ curves should render a straight line through the origin when dislocation slip is the main deformation mechanism contributing to the strain hardening. So, the slope of the straight line would be sensitive to the crystallographic texture of samples since it corresponds with Θ_h , which explicitly depend on the Taylor factor (Cáceres and Blake, 2007; Kocks and Mecking, 2003). The $(\sigma - \sigma_0) \frac{d\sigma}{d\varepsilon} - (\sigma - \sigma_0)$ curves are shown in Figure 14 along with the curves corresponding to the as-extruded L-xHAP composites obtained from the data reported elsewhere (del Campo et al., 2014). The plot for the pure S-Mg sample exhibits a lineal region represented by a straight line that intercepts the abscise axis at ~ 20 MPa, see Figure 14a). This indicates that twinning significantly contribute to the initial strain hardening (Cáceres et al., 2008). Increasing the HA fraction in the S-xHAP composites the Θ_h value is progressively reduced and the interception on the abscise axis shifts towards the origin. This behavior can be considered as evidence for a gradual weakening of the twinning contribution to the strain hardening (Cáceres et al., 2008; Kocks and Mecking, 2003), as Figure 15 supports. The same behavior is observed for the L-xHAP composites in the as-extruded condition, and after ECAP deformation, i.e. for LE-xHAP samples.

Furthermore, it is also evident that the ECAP processing induces an additional reduction of the strain hardening rate Θ_h as the curves of Figures 14b) and c) and the values given in Table 1 reveal. These Θ_h values are found linearly correlated with the inverse of the texture index J^{-1} , as Figure 16 reveals. This is clear evidence for weakening of the texture hardening in extruded magnesium by HA addition as well as by ECAP processing. Such $\Theta_h \propto J^{-1}$ dependence would be expected if texture hardening is effective since it reflects the volume fraction of sample, or number of grains, contributing to the observed strain hardening behavior, i.e. with favorable orientation for dislocation slip. Note that the texture index J derives from the integration of the ODF, which conveys the grain fraction for each specific orientation in a polycrystalline sample. Moreover, it is to be observed that the relationship between number of oriented grains and J^{-1} should lead to an asymptotic value for $J=1$, i.e. for grain orientations at random.

Pure S-Mg as well as the composite sample with a HA fraction of 5% exhibit Θ_h values of 3.30 and 3.17 GPa, respectively. These strain hardening rate values can be representative of pyramidal $\langle c+a \rangle$ dislocation slip in combination with prismatic and basal $\langle a \rangle$ slip according with the results reported for textured Mg samples (Cáceres and Lukác, 2008). After the ECAP processing of the Mg/HA composites and consequent reduction of the texture to J values under 2, the strain hardening rate turns into $\Theta_h \sim 1$ GPa, what should correspond to pure basal $\langle a \rangle$ slip in untextured pure Mg (Cáceres and Blake, 2007; Cáceres and Lukác, 2008). In fact, Θ_h values as small as ~ 0.9 GPa have been reported for random polycrystalline Mg tested under uniaxial compression (Cáceres and Blake, 2007).

The inhibition of the mechanical twinning by the HA phase is tentatively attributed to the capability of the HA particle for blocking the twin propagation in the matrix, what would lead to an early activation of the dislocation slip to accommodate the plastic deformation.

Finally, a plausible explanation for the microhardness dependence on J^{-1} shown in Figure 13 may be given as follows. Microhardness, as a simple measurement of the material resistance to local plastic flow, has to be correlated with the flow stress. In

particular, it appears that the microhardness values for f.c.c. and b.c.c. materials exhibit a grain size dependence similar to the experimental Hall-Petch relationship describing the grain size effect on the flow stress σ , i.e.:

$$\sigma = \sigma_o + k_H D^{-1/2} \quad (2)$$

where D is the mean grain size, σ_o the lattice friction stress and k_H the Hall-Petch slope. There exist models for polycrystalline samples predicting a linear texture dependence of k_H and σ_o via the effective Taylor orientation factor M , that is to say, k_H and $\sigma_o \propto M$, besides being temperature, strain rate and strain dependent (Armstrong et al., 1962; Conrad, 2004). Specifically, the experimental evidence for the dependence of k_H on the type and intensity of the texture have been reported for pure Mg (Wilson and Chapman, 1963; Sambasiva Rao and Prasad, 1982; Wilson, 1970; Cáceres et al., 2008). In this case, it was found that the Hall-Petch slope k_H increases when the texture intensity weakens, and results in the highest value for random oriented polycrystals. If it is tentatively assumed that the microhardness H_V for Mg alloys also exhibit a Hall-Petch relationship as

$$H_V = H_{oV} + KD^{-1/2} \quad (3)$$

where K and H_{oV} would maintain dependences on texture and strain rate comparable to those for k_H and σ_o , then Equation (2) renders H_V values that scale up with the effective Taylor factor M . As the M values for pure Mg increase with reducing texture intensity, the H_V values would scale up with the reciprocal of the texture index J^{-1} when grain size of the sample remains constant. Since the grain size measurements given in Table 1 do not render a Hall-Petch relationship for the yield strength because of the undecided change in the grain sizes, the microhardness dependence on J^{-1} shown in Figure 13 would reflect the effect of the texture. Moreover, the slope change for $J \leq 2$ appears to be correlated with the change in the dislocation slip mechanism.

4. Conclusions

The following remarkable conclusions have been drawn from the present study:

- The microstructural analysis and mechanical characterization of the Mg/HA produced by conventional extrusion have revealed the capability of HA for strengthening and inhibiting the extrusion induced texture, reducing the microstructural anisotropy and preventing the deformation twinning of Mg.
- The ECAP processing applied to these composites, besides enhancing the grain structure and destroying the initial fiber texture, leads to a significant enhancement of their yield strength and microhardness and a consequent reduction of the UCS values.
- The analysis of the athermal strain hardening rate of the flow curves under uniaxial compression at room temperature demonstrates that the HA addition and the ECAP processing are effective for inhibiting non-basal dislocation slip, what produces the observed impairing in the UCS.
- The relationship found between athermal strain hardening rate and texture index indicates that texture hardening controls the dislocation slip responsible for the strain hardening behavior of the Mg/HA composites investigated.

Acknowledgements

This work has been supported by the Regional Government of Madrid through the S2013/MIT-2862-MULTIMAT-CHALLENGE Program. R del Campo thanks to the Universidad Carlos III de Madrid for the support.

References

- Armstrong, R.W., Codd, I.R., Douthwaite, M., Petch, N.J., 1962. The plastic deformation of polycrystalline aggregates. *Phil. Mag.* 7, 45-48.
- Atrens, A., Liu, M., Abidin, N.I.Z., 2011. Corrosion mechanism applicable to biodegradable magnesium implants. *Mater. Sci. Eng. B* 176, 1609-1636.

Barnett, M.R., Keshavarz, Z., Beer, A.G., Atwell, D., 2004. Influence of grain size on the compressive deformation of wrought Mg-3Al-1Zn. *Acta Mater.* 52, 5093-5103.

Bunge, H.J. In: Helga and Hans-Peter Bunge, digital edition, 2015. *Texture analysis in materials science, Mathematical Methods.* Wolfratshausen, pp. 88-90.

Cáceres, C.H., Blake, A.H., 2007. On the strain behavior of magnesium at room temperature. *Mat. Sci. Eng. A* 462, 193-196.

Cáceres, C.H., Lukác, P., 2008. Strain hardening behavior and the Taylor factor of pure magnesium. *Phil. Mag.* 88, 977-989.

Cáceres, C.H., Lukác, P., Blake, A.H., 2008. Strain hardening due to $\{10\bar{1}2\}$ twinning in pure magnesium. *Phil. Mag.* 88, 991-1003.

del Campo, R., Savoini, B., Muñoz, A., Monge, M.A., Garcés, G., 2014. Mechanical properties and corrosion behavior of Mg-HAP composites. *J. Mech. Behav. Biomed. Mater.* 39, 238-246.

Conrad, H., 2004. Grain-size dependence of the flow stress of Cu from millimeters to nanometers. *Metall. Mater. Trans.* 35 A, 2681-2695.

Figueiredo, R.B., Száraz, Z., Trojanová, Z., Lukác, P., Langdon, T.G., 2010. Significance of twinning in the anisotropic behavior of a magnesium alloy processed by equal-channel angular pressing. *Scripta Mater.* 63, 504-507.

Gu, X., Zhou, W., Zheng, Y., Dong, L., Xi, Y., Chai, D., 2010. Microstructure, mechanical property, bio-corrosion and cytotoxicity evaluations of Mg/HA composites. *Mater. Sci. Eng C* 30, 827-832.

Kelley, E.W., Hosford, W.F., 1968. Plane-strain compression of magnesium and magnesium alloy crystals. *Trans. Metall. Soc. AIME* 242, 6-13.

Kocks, U.F., Mecking, H., 2003. Physics and phenomenology of strain hardening: the FCC case. *Prog. Mater. Sci.* 48, 171-273.

Li, Z., Gu, X., Lou, S., Zheng, Y., 2008. The development of binary Mg-Ca alloys for use as biodegradable materials within bone. *Biomaterials* 29, 1329-1344.

- Mensah-Darkwa, K., Gupta, R.K., Kumar, D., 2013. Mechanical and corrosion properties of magnesium-hydroxyapatite composite thin films. *J. Mater. Sci. Technol.* 29, 788-794.
- Neubert, V., Stulikova, I., Smola, B., Mordike, B.L., Vlach, M., Bakkar, A., Pelcova, J., 2007. Thermal stability and corrosion behavior of Mg-Y-Nd and Mg-Tb-Nd alloys. *Mat. Sci. Eng. A* 462, 329-333.
- Sambasiva Rao, G., Prasad, Y.V.R.K., 1982. Grain boundary strengthening in strongly textured magnesium produced by hot rolling. *Metall. Trans. A* 13, 2219-2226.
- Sarker, D., Friedman, J., Chen, D.L., 2015. De-twinning and texture change in an extruded AM30 magnesium alloy during compression along normal direction. *J. Mater. Sci. Technol.* 31, 264-268.
- Song, G., 2007. Control of biodegradation of biocompatible magnesium alloys. *Corros. Sci.* 49, 1696-1701.
- Staiger, M.P., Pietak, A.M., Hadmail, J., Dias, G., 2006. Magnesium and its alloys as orthopedic materials: A review. *Biomaterials* 27, 1728-1734.
- Sun, M., Wu, G., Wang, W., Ding, W., 2009. Effect of Zr on the microstructure, mechanical properties and corrosion resistance of Mg-10Gd-3Y magnesium alloy. *Mat. Sci. Eng. A* 523, 145-151.
- Virtanen, S., 2011. Biodegradable Mg and Mg alloys: Corrosion and biocompatibility. *Mater. Sci. Eng. B* 176, 1600-1608.
- Wilson, D.V., Chapman, J. A., 1963. Effects of preferred orientation on the grain size dependence of yield strength in metals. *Phil. Mag.* 8, 1543-1551.
- Wilson, D. V., 1970. Ductility of polycrystalline magnesium below 300 K. *J. Inst. Metals* 98, 133.
- Witte, F., 2010. The history of biodegradable magnesium implants: A review. *Acta Biomater.* 6, 1680-1692.

Witte, F., Feyerabend, F., Maier, P., Fischer, J., Störmer, M., Blawert, C., Dietzel, W., Hort, N., 2007. Biodegradable magnesium-hydroxyapatite metal matrix composites. *Biomaterials* 28, 2163-2174.

Witte, F., Hort, N., Vogt, C., Cohen, S., Kainer, K.U., 2008. Degradable biomaterials based on magnesium corrosion. *Curr. Opin. Solid State Mater. Sci.* 12, 63-72.

Witte, F., Kaese, V., Haferkamp, H., Switzer, E., Meyer-Linderberg, A., Wirth, C.J., Windhagen, H., 2005. In vivo corrosion of four magnesium alloys and the associated bone response. *Biomaterials* 26, 3557-3563.

Figure captions

Figure 1. Reference system for the samples with Z-axis along the extrusion direction.

Figure 2. Optical microscopy images from pure S-Mg and S-xHAP composites in the as-extruded conditions.

Figure 3. BSE-SEM images of a) S-5HAP, b) S-10HAP and c) S-15HAP in the as-extruded conditions. Figure 3d) SE-SEM of S-10HAP with detail of the boundary grains.

Figure 4. Experimental pole figures for S-Mg, S-5HAP, S-10HAP and S-15HAP in the as-extruded conditions for $(10\bar{1}0)$, (0002) and $(11\bar{2}0)$.

Figure 5. Calculated ODFs for S-Mg and the S-15HAP composite.

Figure 6. Optical microscopy images for Mg/HAP composites ECAP processed (LE-xHAP) for 4 passes via route B_C.

Figure 7. BSE-SEM images of a) LE-5HAP, b) LE-10HAP and c) LE-15HAP processed for 4 passes via route B_C. Fig. 6d) SE-SEM of LE-10HAP with detail of the boundary grains.

Figure 8. Experimental pole figures for Mg/HAP composites ECAP processed (LE-xHAP) for 4 passes via route B_C for $(10\bar{1}0)$, (0002) and $(11\bar{2}0)$.

Figure 9. Calculated ODFs for the LE-5HAP and LE-15HAP composites.

Figure 10. Compressive stress-strain curves for pure Mg and S-xHAP composites extruded at the same conditions.

Figure 11. Compressive stress-strain curves for pure Mg and ECAP processed LE-xHAP composites extruded at the same conditions.

Figure 12. HA content effect on the microhardness of the Mg/HAP composites on (X-Y) and (X-Z) sections.

Figure 13. Relationship between microhardness and texture index J for Mg/HAP composites on (X-Y) and (X-Z) sections.

Figure 14. Kocks-Mecking plots showing the strain hardening behavior for the Mg/HAP composites.

Figure 15. Optical images showing deformation twinning for a) pure Mg and b) S-15HAP composite.

Figure 16. Athermal strain hardening rate versus J^{-1} for pure magnesium and magnesium/HAP composites.

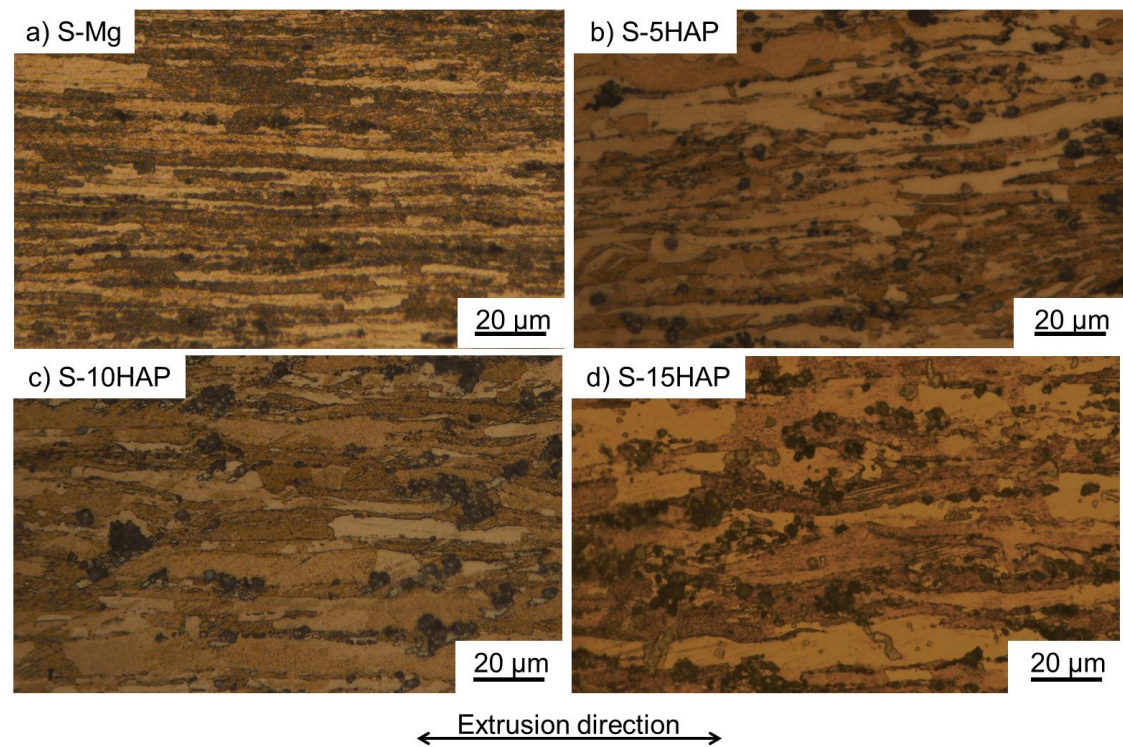
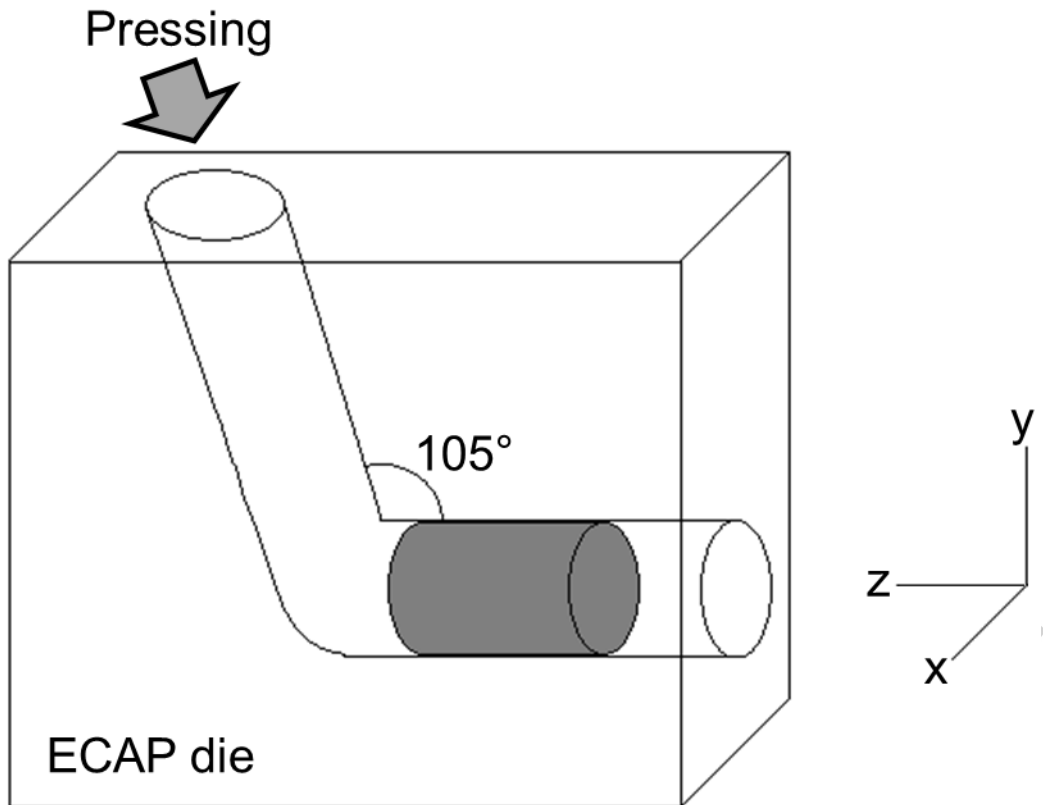
Table 1 Microstructural and mechanical characteristics for Mg/HAP composites

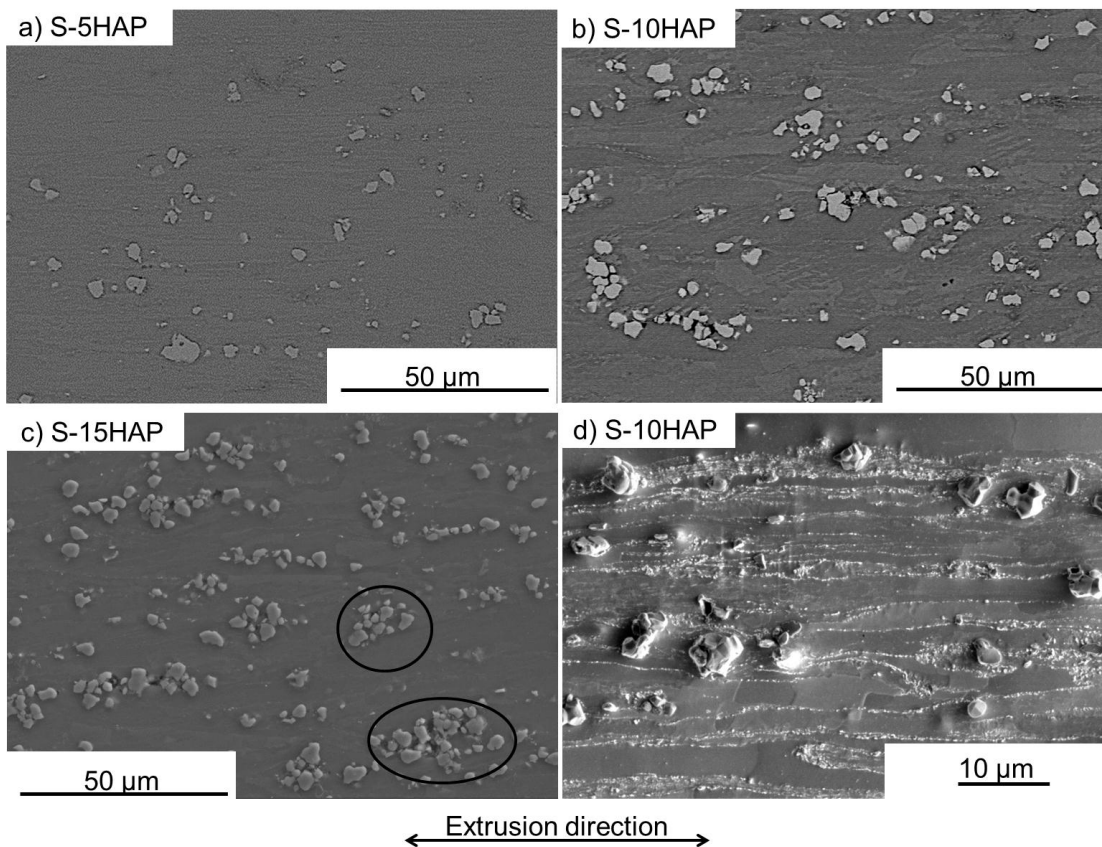
Sample	ρ/ρ_{cal} (%)	Grain length (μm)	Grain width (μm)	Aspect ratio	J Texture index	$H_v(T)$ (MPa)	$H_v(L)$ (MPa)	YS (MPa)	UCS (MPa)	Uniform strain (%)	Θ_h (GPa)
S-Mg	98.8±0.2	37±17	2.6±1.0	14	5.55	523±5	500±7	189	296	0.09	3.30
S-5HAP	98.9±0.2	30±16	4.2±1.5	7	3.85	543±7	520±5	202	329	0.10	3.17
S-10H	96.9±0.2	41±23	5.4±1.7	8	2.70	559±7	540±7	205	334	0.13	1.91

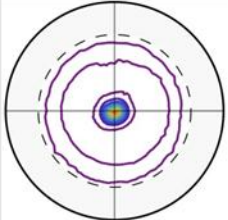
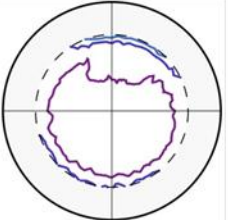
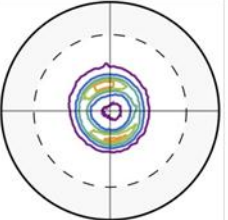
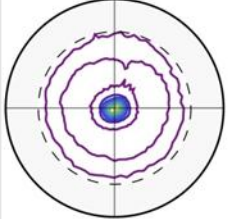
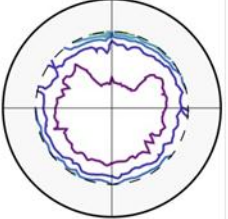
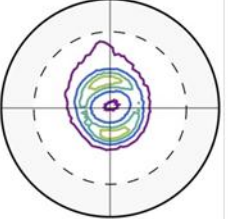
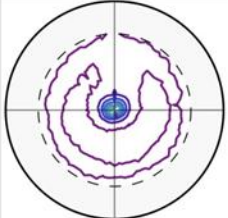
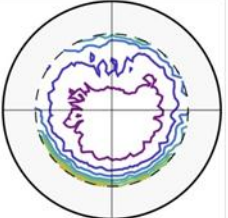
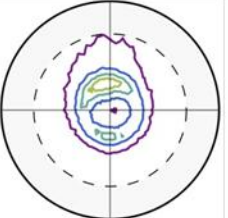
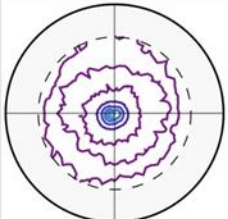
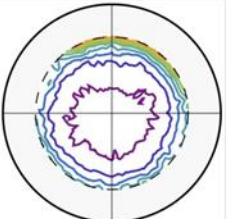
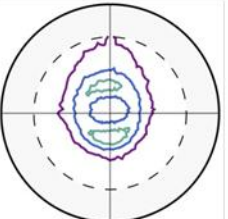



AP												
S-	96.4±	27±	4.8±			585±	570±					1.6
15H	0.2	17	1.7	6	2.20	8	10	207	348	0.14		5
AP												
LE-	97.7±	19±	5.8±			586±	590±					1.0
5HA	0.2	7	2.3	3	2.00	3	10	231	355	0.17		7
P												
LE-	97.6±	10±	4.1±			640±	621±					1.1
10H	0.2	6	1.5	2	1.85	20	7	235	342	0.13		0
AP												
LE-	98.0±	9±4	4.7±			690±	680±					0.7
15H	0.2		1.2	2	1.65	20	20	237	326	0.13		9
AP												
L-	96.4±	25±	5.2±			560±	530±					3.4
5HA	0.2	15	2.3	5	5.70	10	10	213	449	0.14		5
P												
L-	96.0±	29±	5.5±			593±	580±					2.3
10H	0.2	18	2.0	5	3.30	7	10	215	410	0.15		7
AP												
L-	94.0±	32±	6±5			623±	610±					1.8
15H	0.3	17		5	2.20	9	10	222	373	0.12		3
AP												

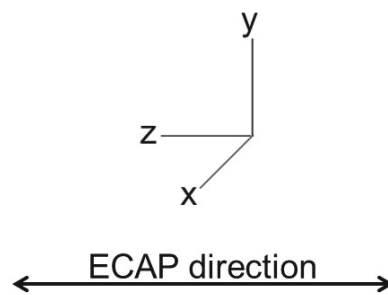
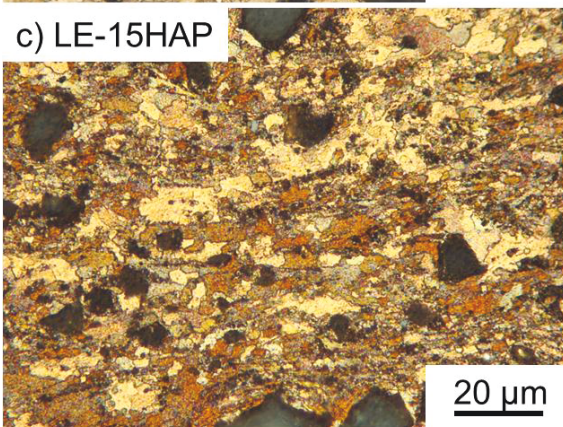
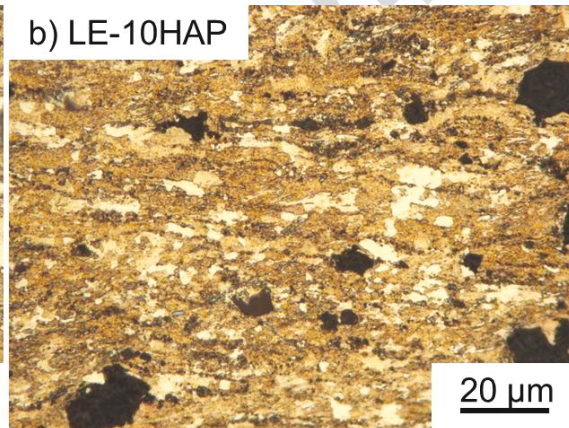
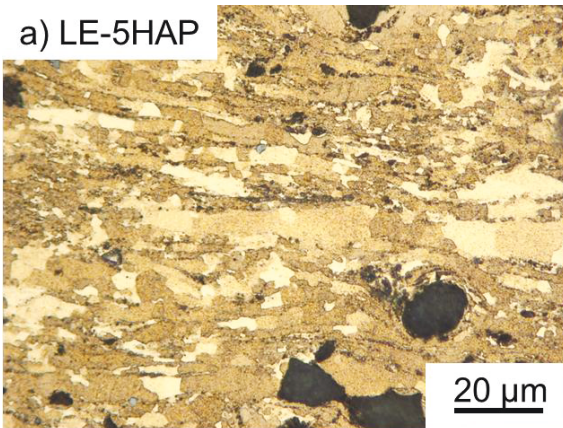
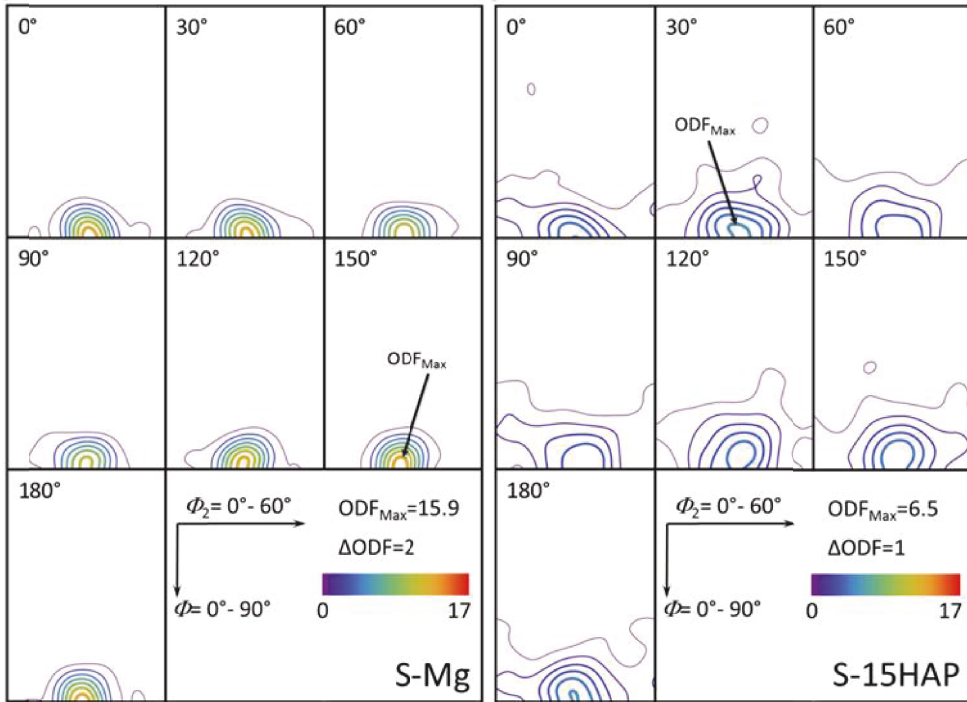
Highlights

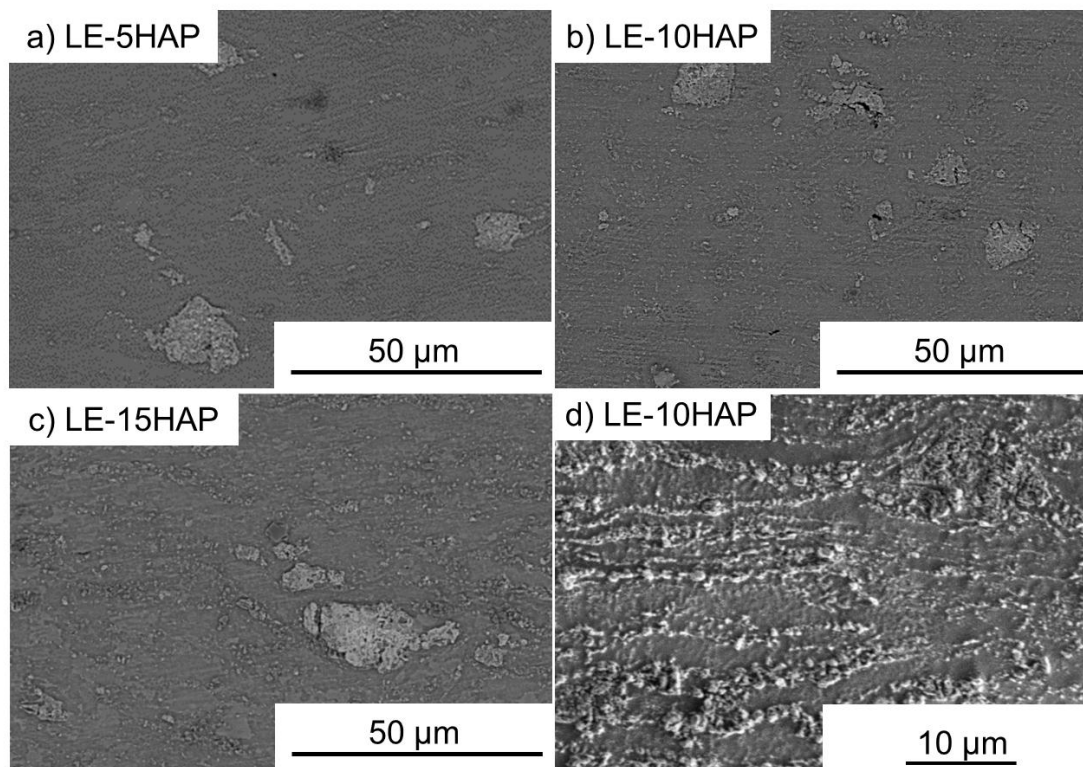
- Mg-HAP composites were produced by a powder metallurgy followed by extrusion and ECAP.
- The HAP addition to Mg enhances compressive strength, reduces extrusion texture and prevents deformation twinning.
- ECAP deformation of these composites destroys the initial texture and improves yield strength and microhardness.
- A lineal correlation is found between athermal strain hardening rate and inverse of texture index.





Material	$(10\bar{1}0)$	(0002)	$(11\bar{2}0)$	Texture Index J
S-Mg				5.55
S-5HAP				3.85
S-10HAP				2.70
S-15HAP				2.20
Scale (r.m.d.)	 0 24.0	 0 4.4	 0 8.4	





Material	$(10\bar{1}0)$	(0002)	$(11\bar{2}0)$	Texture Index J
LE-5HAP				2.00
LE-10HAP				1.85
LE-15HAP				1.65
Scale (r.m.d.)	0 4.1	0 5.5	0 4.6	

